Naval Research Laboratory

Design and Initial Operation of a 6 kW 2.45 GHz Single-Mode Microwave Cavity Furnace

ARNE W. FLIFLET

Beam Physics Branch
Plasma Physics Division

RALPH W. BRUCE

Electrical Engineering Department
United States Naval Academy

DAVID LEWIS, III
ROY RAYNE
BARRY BENDER

Mechanics of Materials Branch
Materials Science and Technology Division
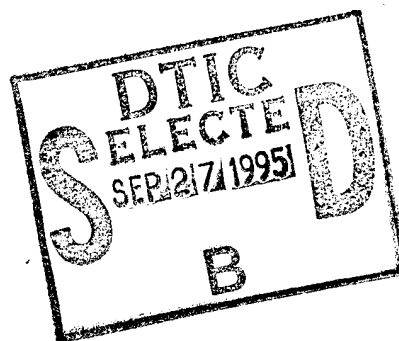
LYNN K. KURIHARA
GAN-MOOG CHOW
PAUL E. SCHOEN

Center for Biomolecular Science and Engineering

ALLEN K. KINKEAD

Sachs Freeman Associates
Landover, MD

September 1, 1995

REPORT DOCUMENTATION PAGE

1. AGENCY USE ONLY (Leave Blank)	2. REPORT DATE September 1, 1997	3. REPORT TYPE AND DATES COVERED Interim	

4. TITLE AND SUBTITLE

Design and Initial Operation of a 6 kW 2.45 GHz Single-Mode Microwave Cavity Furnace

5. FUNDING NUMBERS

67-M038-B-5

6. AUTHOR(S)

A.W. Fliflet, R.W. Bruce,* D. Lewis, III, R. Rayne, B. Bender, L.K. Kurihara,† G.-M. Chow, P.E. Schoen, and A.K. Kinkead**

7. PERFORMING ORGANIZATION NAME(S) AND ADDRESS(ES)

Naval Research Laboratory
Washington, DC 20375-5320

8. PERFORMING ORGANIZATION REPORT NUMBER

NRL/MR/6793--95-7745

9. SPONSORING/MONITORING AGENCY NAME(S) AND ADDRESS(ES)

Office of Naval Research
800 North Quincy Street
Arlington, VA 22217-5660

10. SPONSORING/MONITORING AGENCY REPORT NUMBER

11. SUPPLEMENTARY NOTES

*U.S. Naval Academy, Annapolis, MD   †NRL/ASEE Post Doc
**SFA, Landover, MD

12a. DISTRIBUTION/AVAILABILITY STATEMENT

Approved for public release; distribution unlimited.

12b. DISTRIBUTION CODE

13. ABSTRACT (Maximum 200 words)

A single-mode cavity microwave furnace, operating in the TE_{103} mode at 2.45 GHz, has been set up at the Naval Research Laboratory (NRL) and is currently being used to investigate sintering of nanocrystalline ceramics. This memorandum will discuss the apparatus used and the results obtained to date. The high purity Al_2O_3 and TiO_2 nanocrystalline powders were first uniaxially pressed to 14 MPa, cold isostatically pressed (CIP'ed) to various pressures $\geq$ 420 MPa and finally sectioned into wafers. The density of the green compacts was 30 to 38% theoretical density (TD). The compacts were placed in insulating fiberboard caskets which were lossy enough at room temperature to provide hybrid heating. At temperatures above 600°C the compacts were heated primarily by the microwave radiation. The wafers were heated in the microwave furnace for up to three hours at temperatures $\leq$ 1720°C. The temperature of the workpiece was monitored using an optical pyrometer. Final densities up to 80% TD have been obtained to date for Al_2O_3 and up to 52% TD for TiO_2. The sintered compacts were characterized by x-ray diffraction and by scanning electron microscopy to determine the phase and grain size.

14. SUBJECT TERMS

Microwave
Sintering
Ceramics

15. NUMBER OF PAGES

23

16. PRICE CODE

17. SECURITY CLASSIFICATION OF REPORT UNCLASSIFIED	18. SECURITY CLASSIFICATION OF THIS PAGE UNCLASSIFIED	19. SECURITY CLASSIFICATION OF ABSTRACT UNCLASSIFIED	20. LIMITATION OF ABSTRACT UL

CONTENTS

INITIAL OPERATION OF A 6 kW 2.45 GHz SINGLE-MODE MICROWAVE CAVITY FURNACE

I. Introduction

Microwave processing of advanced ceramic materials is emerging as an important new technology with many advantages compared to conventional processing techniques. These advantages include improved quality, new material properties, and faster processing. An overview of the current state-of-the art in this field is given by the November 1993 issue of the *Bulletin of the Materials Research Society*.[1] In conventional heating of ceramic materials, energy is applied at the surface of the workpiece by flowing gas or infrared radiation and is transferred into the bulk by conduction. This process is relatively slow (the processing time is usually measured in hours), often produces internal stresses in the material due to nonuniform heating, and is often accompanied by significant grain growth which reduces material performance. In contrast, microwave heating deposits energy far more rapidly and volumetrically, and can result in little grain growth. On the other hand, since the microwave absorption rate is highly temperature dependent and ceramic materials usually have low heat conductivity, the heating process is prone to temporal and spatial thermal runaway. In addition, microwave absorption of 2.45 GHz radiation (the frequency of conventional microwave ovens) at room temperature is so low for many ceramic materials that heating can not be achieved without used hybrid (conduction + microwave) heating techniques. In order to investigate methods of overcoming these limitations, and to provide a basis for comparison with planned high frequency microwave heating experiments, an S-band 2.45 GHz microwave resonant cavity furnace operating in the TE_{103} mode has been set up at the Naval Research Laboratory (NRL). This memorandum describes the design and operating parameters of the microwave furnace and reports on preliminary sintering experiments carried out on green compacts of nanocrystalline alumina and titania.

The single-mode resonant cavity configuration was chosen for its simple, well-characterized field structure and ability to produce high fields. In contrast, the conventional microwave oven is highly overmoded, making it more difficult to model. The field pattern in the TE_{103} mode cavity was considered to be sufficiently uniform at the field maximum for heating small samples with dimensions up to a few cm's. Section II gives a brief introduction to the theory of microwave loss mechanisms in ceramic materials. A fairly detailed discussion of the microwave system design is given in Section III as a review of the literature indicates that this does not appear to be readily available. Section IV presents the results of preliminary sintering experiments.

II. Loss Mechanisms in Ceramic Materials

Microwave heating of a dielectric can result from conduction currents associated with free charge carriers or from displacement currents associated with polarization relaxation. The conductivity of polycrystalline ceramic insulator is very low near room temperature but increases exponentially at higher temperatures, either through the promotion of electrons into conduction bands, or through the diffusion of ions through the lattice. Displacement currents are associated with the onset of polarization, of which there are several types, each having a characteristic response time τ. Displacement polarization is associated with the response of bound electrons and ions to the applied field. Electronic displacement polarization is established very quickly compared to the period of microwave radiation ($\tau \sim 10^{-14} - 10^{-15}$ s) and does not contribute energy dissipation at microwave frequencies. Ionic displacement polarization is established on an infrared time scale ($\tau \sim 10^{-12} - 10^{-13}$ s) and also contributes little to losses at microwave frequencies. Orientational polarization associated with thermal motion is established on a slower time scale and can result in significant losses at microwave frequencies. Orientational polarization of materials made of polar molecules was first treated by Debye. Alternatively, in a polycrystalline solid, the presence of impurities can lead to polarization through the formation of weakly bound impurity ion–lattice vacancy pairs. Such ions–vacancy pairs have a dipole moment which can be reoriented when the impurity ion moves between equivalent sites through thermal motion. The ability of impurity ions and vacancies to "jump" between sites depends on the strength of bonding to the lattice and on the temperature of the material. Application of an external field leads to polarization by establishing a preferred direction for the otherwise random thermal motion of these ions. The concentration and mobility of these ions are usually low in pure oxide ceramics at room temperature. However, impurities and lattice defects are concentrated near the grain boundaries of polycrystalline ceramics, so that impurity ion absorption may be particularly important for ultra-fine grain ceramics due to their large surface-to-volume ratio.

The total current density flowing in a dielectric due to an applied electric field is the sum of the conduction and polarization currents:

$$j = j_c + j_p = \sigma E + \frac{\partial \mathcal{P}}{\partial t} \tag{II.1}$$

Following the sudden application of a constant field, the polarization can be expressed in the following form:

$$\mathcal{P}(t) = \mathcal{P}_\infty + \left(\mathcal{P}_s - \mathcal{P}_\infty\right)\left(1 - e^{-t/\tau}\right) \tag{II.2}$$

2

where $\mathcal{P}_\infty$ is the instantaneous polarization on applying the field (in this case ionic and electronic displacement polarization), $\mathcal{P}_s$ is the final value established by a constant applied electric field, and τ is the relaxation time constant. The relaxation polarization current for a constant applied field is therefore:

$$j_\tau = ge^{-t/\tau}E \tag{II.3}$$

where

$$g = \frac{\varepsilon_0\left(\kappa_s - \kappa_\infty\right)}{\tau} \tag{II.4}$$

κ_s and κ_∞ are the relative final and instantaneous permittivities, and ε_0 is the free-space permittivity. To obtain the relaxation polarization current for a sinusoidal field, $E = E_m e^{i\omega t}$, consider the increase in current due to a sudden increase in the field at t_0

$$\Delta j_\tau = ge^{-\frac{t-t_0}{\tau}}\Delta E \tag{II.5}$$

and apply the principle of superposition of currents (which states that the total current passing at a given moment through a dielectric after a series of voltage changes is equal to the sum of the current increments due to each of the preceding voltage changes).[2] This leads to the following expression

$$j_\tau = g\int_{-\infty}^{t} \frac{dE}{dt'}e^{-\frac{t-t'}{\tau}}dt' \tag{II.6}$$

Evaluating this integral and adding the contribution from the instantaneous polarization, the total polarization current for a sinusoidal field is given by

$$j_p = \frac{\omega^2\tau\varepsilon_0\left(\kappa_s - \kappa_\infty\right)}{1+\omega^2\tau^2}e^{i\omega t}E_m + i\omega\varepsilon_0\left(\kappa_\infty + \frac{\left(\kappa_s - \kappa_\infty\right)}{1+\omega^2\tau^2}\right)e^{i\omega t}E_m \tag{II.7}$$

The first term is the active component of the polarization current (in phase with the rf electric field), and the second term is the reactive (capacitive) component (leads the rf field by a phase angle $\pi/2$). If there is finite conductivity, the active polarization current is supplemented by the conduction current, and the total current density can be expressed in the form

$$j = \left(j_a + ij_r\right)e^{i\omega t} \tag{II.8}$$

where

3

$$j_a = \sigma E_m + \frac{\omega^2 \tau \varepsilon_0 \left(\kappa_s - \kappa_\infty \right)}{1 + \omega^2 \tau^2} E_m \tag{II.9}$$

and

$$j_r = \omega \varepsilon_0 \left(\kappa_\infty + \frac{\left(\kappa_s - \kappa_\infty \right)}{1 + \omega^2 \tau^2} \right) E_m. \tag{II.10}$$

The conduction and relaxation losses per unit volume and per unit time are given by

$$p = \frac{j_a E_m}{2} = \omega \varepsilon_0 \left(\frac{\sigma}{\omega \varepsilon_0} + \frac{\left(\kappa_s - \kappa_\infty \right) \omega \tau}{1 + \omega^2 \tau^2} \right) \frac{E_m^2}{2} \tag{II.11}$$

The polarization can be expressed in terms a complex permittivity

$$\mathcal{P} = \varepsilon_0 \kappa^* E \tag{II.12}$$

where

$$\kappa^* = \kappa' - i \kappa'' = \kappa_\infty + \frac{\kappa_s - \kappa_\infty}{1 + \omega^2 \tau^2} - i \frac{\left(\kappa_s - \kappa_\infty \right) \omega \tau}{1 + \omega^2 \tau^2} \tag{II.13}$$

The loss tangent for relaxational and conduction losses is then given by

$$\tan \delta = \frac{j_a}{j_r} = \frac{\kappa'' + \dfrac{\sigma}{\varepsilon_0 \omega}}{\kappa'} = \frac{\dfrac{\sigma}{\varepsilon_0 \omega} \left(1 + \omega^2 \tau^2 \right) + \left(\kappa_s - \kappa_\infty \right) \omega \tau}{\kappa_s + \kappa_\infty \omega^2 \tau^2} \tag{II.14}$$

The present analysis assume that there is only one relaxation time whereas is general there may be a distribution of such relaxation times. Eq.(II.11) for the dissipated power can be expressed in the well-known form

$$p = \omega \varepsilon_0 \kappa' \tan \delta \frac{E_m^2}{2} \tag{II.15}$$

The foregoing analysis shows that both relaxation and conduction processes contribute to microwave losses in ceramics. Both mechanisms tend to be small in many pure ceramics at ambient temperature, but increase rapidly above some critical temperature — usually several hundred °C. For example, in a ceramic with an ionic crystal structure, the conductivity is proportional to the ion diffusion coefficient D, which has an exponential temperature dependence of the form:

4

$$D = D_0 e^{-E/kT} \qquad\qquad\qquad (\text{II}.16)$$

where E is the activation energy of diffusion, T is the temperature, k is the Boltzman coefficient, and D_0 is a temperature-independent factor. Above a critical temperature determined by the activation energy, this becomes the dominant loss mechanism and the loss tangent assumes an exponential temperature dependence. This dependence leads to the well-known thermal runaway effect in microwave heating of ceramics. Microwave losses in polycrystalline ceramics tend to increase with decreasing grain size since diffusion processes are enhanced near the grain surface. Thus nanocrystalline ceramics are expected to be more lossy than conventional micron grained ceramics. This trend has been shown in loss tangent measurements for alumina.[3]

III. The Microwave Furnace

The basic configuration of the microwave furnace system is show in Fig. 1 and consists of a microwave source, waveguide transmission and control devices, a single-mode resonant cavity, and power and temperature sensors. The purpose of the microwave cavity and associated hardware is to maximize the electric field at the workpiece and optimize the microwave coupling efficiency. As the workpiece heats, its electrical properties change, as discussed in Section II, and it is necessary to adjust the cavity dimensions to maintain resonance and effective power coupling. The order of presentation will be to first describe the furnace cavity, then the source, and finally the transmission, control and power sensing systems.
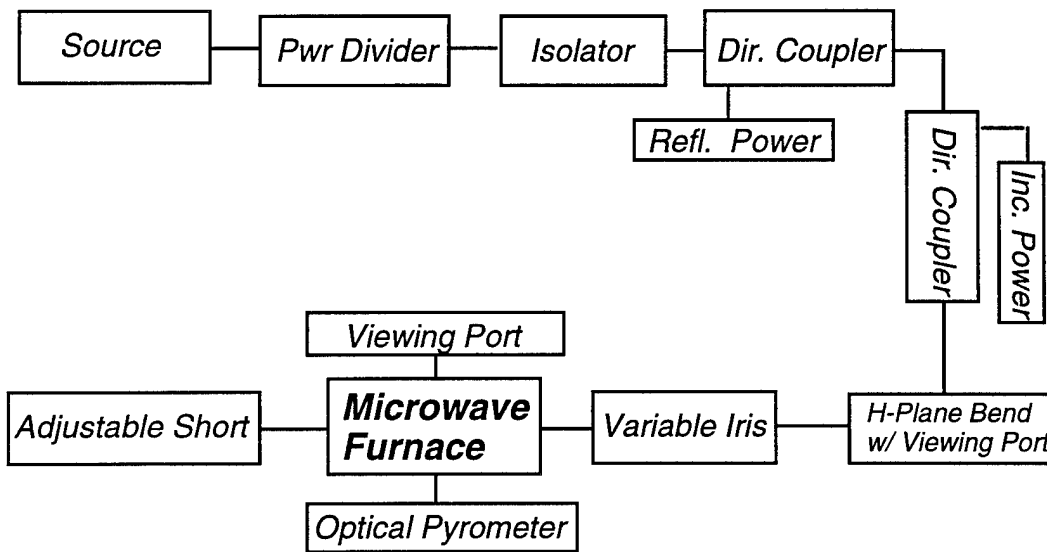

Figure 1: Microwave Furnace System

III.A   Single-Mode Resonant Cavity Furnace

The microwave cavity, shown schematically in Figure 2, is designed to support the TE$_{103}$ rectangular waveguide mode and is constructed from WR-284 copper waveguide (a = 7.21 cm, b = 3.40 cm). There is an adjustable diaphragm (iris) at one end for power input, and a sliding short at the other. The design of this furnace is based on the work of Aliquat, Mazo, and Desgardin.[4] The guide wavelength at 2.45 GHz in WR-284 is λ_g = 23.12 cm and the total length of the furnace cavity is approximately l =1.5λ_g = 34.8 cm. Two holes (3.5 cm diameter) were put in the top and bottom broadwalls at 17.50 cm from the source end as material loading ports. This position was chosen to insure that the work piece would be near a field maximum at resonance. On both sidewalls at the same position, additional ports (1.4 cm diameter) were made and are used as viewing and sensing ports. Copper tubing was soldered to the outside to provide cooling of the cavity walls [Figure 2]. The top and side ports were designed to allow the attachment of various tubes, caps, etc., for sensing and viewing. They were also designed so that the cavity could be evacuated, back-filled or pressurized depending upon the type of atmosphere needed for sintering.
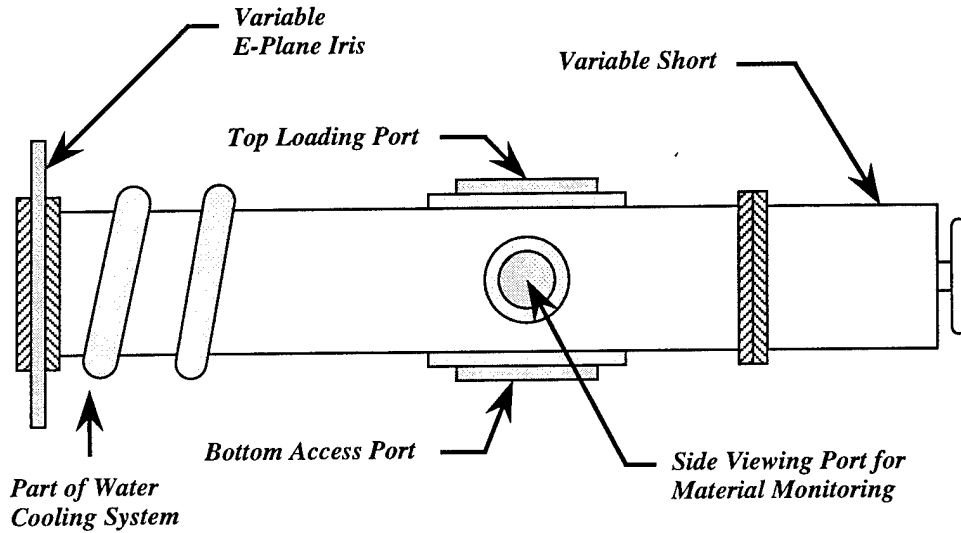

Variable E-Plane Iris

Variable Short

Top Loading Port

Bottom Access Port

Side Viewing Port for Material Monitoring

Part of Water Cooling System

Figure 2: Schematic of 2.45 GHz single-mode microwave furnace

The iris at the cavity input acts as a shunt inductive element for the TE$_{10}$ mode. The normalized inductive susceptance (corresponding to a transmission line with unit characteristic impedance) for a symmetric diaphragm is given approximately by:[5]

$$\overline{B} = \frac{\lambda_g}{a}\cot^2\frac{\pi d}{2a}\left(1+\frac{a\gamma_3 - 3\pi}{4\pi}\sin^2\frac{\pi d}{a}\right) \qquad \text{(III.1)}$$

where d is the width of the diaphragm opening and $\gamma_3 = \sqrt{(3\pi/a)^2 - k_0^2}$. The cavity Q factor for the diaphragm is given by

$$Q_d = \frac{\pi d \lambda_g}{\lambda^2}\left(\bar{B}^2 + 1\right) \qquad (III.2)$$

In the present experiments the ceramic workpiece was typically a disk or rectangular slab oriented in the x-y plane of the cavity at a field maximum. Since the TE$_{10}$ mode electric field is tangential to the workpiece surface, it is continuous at the boundary and so for a thin disk or rectangular slab, the electric field in the workpiece is approximately equal to the field outside the workpiece. From Eq.(II.15) the microwave power absorbed by the workpiece is:

$$P_L = 2\pi\varepsilon_0 f \kappa' \tan\delta \left|E_0\right|^2 V_L \qquad (III.3)$$

where f is the microwave frequency, V_L is the workpiece volume, and E$_0$ is the RMS electric field amplitude in the cavity. The Q factor for the load is given by:

$$Q_L = \frac{abl}{4\varepsilon' \tan\delta V_L} \qquad (III.4)$$

The internal Q factor for the cavity is:

$$Q_0 = \left[\frac{1}{Q_L} + \frac{1}{Q_c}\right]^{-1} \qquad (III.5)$$

where Q_c is the Q of the empty cavity and accounts for ohmic losses on the cavity surfaces and at cracks associated with the short, iris, and flanges. The cavity efficiency (fraction of the total power absorbed by the cavity transferred to the workpiece) is

$$\eta_c = \frac{Q_0}{Q_L} \qquad (III.6)$$

The cavity coupling parameter is

$$\beta = \frac{Q_0}{Q_d}, \qquad (III.7)$$

the diaphragm power reflection coefficient is given by

$$R = \frac{(1-\beta)^2}{(1+\beta)^2}, \qquad (III.8)$$

7

and the power transfer efficiency to the load (fraction of incident power transmitted to load) is

$$\eta_p = (1 - R)\eta_c \qquad \text{(III.9)}$$

Cold tests were carried out to determine Q_c or the TE$_{103}$ mode at 2450 MHz. The results are shown in Figure 3 as a function of the iris opening. This data shows that Q_c ≈400, which is quite low in comparison with the ohmic Q for an ideal copper cavity. The cavity losses are due to cracks or gaps associated with the sliding short, the broadwall openings in the cavity, and the adjustable iris. Small changes in the position of iris components or the sliding short associated with the play in these mechanical systems were found to cause large variations in these losses. This is assumed to be the cause of the anomalously low Q value shown in Fig.3 for the 1 cm iris opening.
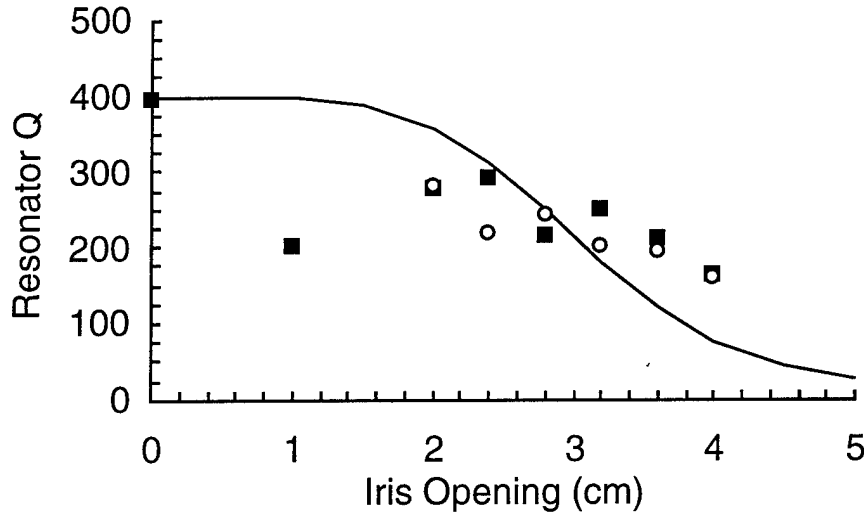

Figure 3: Cold test results for single-mode cavity at 2450 MHz. Solid squares: measured Q of empty cavity, open circles: measured Q of cavity with sample and casket, solid curve: theoretical Q factor normalized to 400 for closed iris.

The green cold-pressed compacts of nanocrystalline alumina and titania studied in this work were typically 2 cm in diameter and 0.5 cm thick. Assuming a permittivity (real part) of 10 and a loss tangent of 0.001, the workpiece Q factor, Q_L~ 3500. This is much less than the empty cavity Q factor and implies that the cavity coupling efficiency is very low, ≈ 10%. Not surprisingly, attempts to heat a compact by itself in the cavity were unsuccessful. Instead, a hybrid technique was used which involved surrounding the compact by a "casket" of alumina or zirconia insulating fiberboard. The Q of the casket-compact system is much less than that of the compact alone in part because of the additional absorbing volume of the fiberboard, and in part because the fiberboard includes a relatively

lossy material as a binder. As shown in Fig. 3, at room temperature the cavity Q is practically unaffected by the presence of the casket and workpiece indicating that $Q_L \geq Q_c$.

Figure 4 demonstrates the need for a variable iris to optimize coupling efficiency during the heating process. The solid curve shows the calculated coupling efficiency of the incident power to the load as a function of iris opening at room temperature. The load (casket plus workpiece) is taken to be 2 cm thick and to completely fill the rectangular cavity. The load loss tangent is assumed to be $\delta = 0.001$. The curve indicates that optimum coupling occurs at an iris opening of 3.7 cm. This behavior is in agreement with the observed operation of the cavity, except that the experimental optimum iris opening at room temperature is ~ 2.8 cm. The dashed curve shows the effect of increasing the loss tangent to $\delta = 0.02$, a value representative of the load at high temperature. In this case, the optimum coupling is obtained with the iris wide open, again in agreement with the observed operation of the furnace.
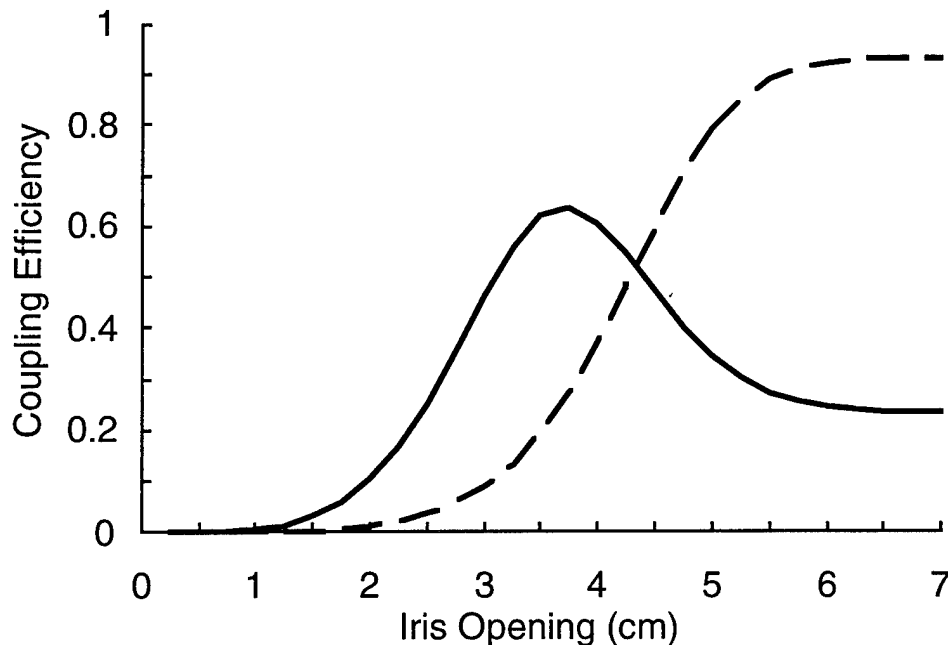

Figure 4: Calculated incident power to load conversion efficiency. Solid curve: room temperature load ($\delta = 0.001$), dashed curve: high temperature load ($\delta = 0.02$).

III.B Cober 2.45 GHz Industrial Microwave Source

The source used for these experiments is the Cober S6F 2.45 GHz industrial microwave source which is rated at 6 kW. Temperatures of over 1900 °C could be reached

at output powers of 1700 W or less. The minimum power available from the unit was effectively 600 W as below this power level, the power would fluctuate. In all cases, the output was a continuous wave (CW), as opposed to the pulsed CW used for power level control in the home microwave oven.

III.C Transmission/Control and Power Sensing System

It took a number of iterations to obtain a transmission, control and power sensing subsystem that was adequate to the task. Initially, the power source was connected directly to the resonant cavity furnace subsystem using various lengths of WR-284 waveguides. One E-plane bend had the capability of monitoring the frequency and a limited capability for power measurement. Power was coupled to the cavity through a 2.54 cm diameter fixed iris. Microwave heating was observed for of a number of materials such as sintered BN and TiO_2, and various insulating ceramic fiber boards such as Zircar SALI™ and ZYZ3™.

The rapid heating of the fiber board materials to temperatures above 1000°C was not expected as these materials are porous (porosity $\geq 80\%$) and consist mainly of alumina or zirconia. Once it was realized that the SALI™ insulation fibers were coated with SiO_2 or that there was a significant fraction of Yttria in the ZYZ3™ causing an marked increase in the conductivity, the cause of the rapid heating was solved. As described below, this proved beneficial in later experiments as the insulation became the mechanism for the hybrid heating of the nanocrystalline materials at low temperatures. The description of this will be given in greater detail in the next section and in the section on results.

The principal problems encountered with this subsystem were associated with control of the incident power at levels below 600 W, monitoring of the forward and reflected power, and the wide variation of the load impedance during heating. Measurement of the forward and reflected power is necessary to monitor power flow into the cavity and to keep the cavity tuned to resonance. The most accurate measurements were obtained with a pair of 20 dB directional couplers. The Cober microwave source could not be operated stably at output powers below 600 W. This required the addition of a variable power divider that could reduce the incident power level to less than 1 W in order to control the onset of heating. In the earlier experiments where power absorbed in the sample was moderated only by the movement of the variable short, the materials temperature would rise very rapidly as the cavity was brought into resonance. With the variable power divider, the cavity could be brought into resonance at low power and the power then raised slowly to more controllably reach the desired temperature. Because the load impedance varies so much during the heating/sintering process, the ability to monitor

how well the source is matched to the cavity is of great importance. A circulator was also added to the system downstream from the power divider since reflected power was found to interfere with the power divider operation. The subsystem configuration is shown in Figure 1.

This present configuration has been adopted to overcome the problem of directivity in waveguide couplers. Directivity is the measure, in dB, of microwave power leakage from the opposite direction from which power is to be sampled. In the ideal case, all power coupled through for power sampling would be from the direction of interest. But due to problems of waveguide asymmetry and wavelength effects due to the wide frequency band of most waveguides, there can be significant power leakage from the unwanted direction. The amount of power is also dependent upon the type of coupler used and the frequency of the source. In all cases, the waveguides used in this system are WR-284 which is designed for the 2.61 to 4.00 GHz band and has center frequency of 3.12 GHz. Therefore the guide wavelength at the operating frequency is much longer than at the center frequency wavelength (23.16 cm vs. 9.63 cm, respectively) resulting in significant phase change differences for the various paths the power flows. Table I compares the measured port-to-port power couplings for the 20 dB cross-guide coupler (HP 750D) with the 20 dB three-port directional coupler (HP 752D).

Under worst case conditions, a total reflection for the forward signal when the cavity is far from resonance, significantly more power from the reflected signal would

Table I. Comparison of 20 dB Couplers

	Cross-Guide (HP 750D)	Directional (HP 752D)
Input to Output Port	-0.53 dB	-0.29 dB
Input to Coupled Port	-21.9 dB	-19.1 dB
Directivity	-24.3 dB	-36.8 dB

flow to the coupled port of the cross-guide coupler than to the coupled port of the standard directional coupler. As an example, for the cross-guide coupler, and an input power of 100 watts, the power from the forward signal would be 0.65 W. If there is total reflection of the forward signal, the amount of power at the coupled port from the reflected signal will be 0.33 W. Since the two signals may be in or out of phase, the measured power at the coupled port will range from 0.32 W to 0.98 W, a ± 50% error. In the case of the HP 752D directional coupler, the values would be 1.23 W from the incident power and 0.02 W from the reflected power. The error is now ± 1.6%. The purpose of this discussion has been to point out the difficulty in accurately measuring the forward power if the coupler is not sufficiently directional. If an analysis is made for the measurement of the reflected power, similar errors in the measured values will occur. When the cavity is well matched

to the subsystem, most of the power read at the reflected port will in fact be due to the energy being coupled from the forward direction rather than the reverse direction (as one would normally expect).

IV. Experimental Results

The sintering of nanocrystalline ceramics using microwaves as the power source has been studied by several groups.[6-12] Nanocrystalline ceramics are of interest for microwave processing because the dielectric loss factor increases significantly as the particle size decreases. Coupled with the fact that the power absorbed by any material is linearly dependent upon the frequency, raising this frequency, from, say, 2.45 GHz to 35 GHz or higher, will also raise the power absorbed.[13] A five year study was begun at NRL in the Fall of 1994, one purpose of which is to investigate microwave processing issues for nanocrystalline materials. The initial phase of this study is to focus on the use of 2.45 GHz microwave power for microwave sintering of ceramics. This effort will be followed by work at higher frequencies using a tunable quasioptical gyrotron (QOG) that will operate in the range 85 to 120 GHz, and a 35 GHz gyrotron.

IV.A Sample Preparation

Nanocrystalline powders were prepared using a modified sol-gel technique. The resulting powders were then filtered, washed with water, and dried. The resulting precursor powders were filtered, washed with distilled deionized water, and dried. The powders were calcined in air at 700°C for 2 hours. The calcined powders were then uniaxially pressed to 14 MPa and cold isostatically pressed (CIP'ed) to 420 MPa. In spite of the fairly high CIP pressure, the density of the green compacts was only 30% TD (theoretical density) for the titania and 37% TD for the alumina. These green compact densities are probably too low for achieving near 100% densification during pressureless sintering. The low densities are attributed to the fact that no binders, surfactants or sintering aids were used. In addition, the green density is affected by the presence of agglomerates. One goal of this investigation was to determine whether pure nanocrystalline materials could be sintered without any form of pressing or sintering aids. Individual samples were then cut using a diamond saw. The samples were placed in a box oven at 200°C until the sintering operation to minimize the absorption of water vapor prior to sintering. The individual samples were then placed into an insulating box ("casket") located at an rf field maximum of the microwave furnace. Runs with various heating profiles were then used to obtain preliminary data on densification rates and achievable final

density. Of the two materials, the titania was more easily heated but, as will be described below, did not achieve final densities as high as the alumina.

IV.B Sintering Experiments

A sufficient number of runs were made using the furnace to ensure that reliable results could be obtained. Some of these results are tabulated in Table II, below. It should be noted from this table that both the alumina and titania were only isostatically pressed to about 30–38% TD. This is in contrast to some work in which the starting TD's were closer to 50% TD.[6,10] Final TD's varied considerably. The first runs for the Al_2O_3 were to determine if these materials could be heated at all in the rather simple casketing system devised. The casketing usually consisted of a cavity hollowed out of Zircar SALI™ or ZYZ3™ fiberboard insulation which also had a lid to ensure that the sample was fully covered. A typical casket configuration is shown in Figure 5. A small hole was made in the widest side so that the surface temperature of the sample could be observed. The sample and casket were placed at the mid-point of the second maximum of the TE_{103} mode. This allowed viewing of the sample through an observation port constructed in the middle of an H-plane bend that was upstream from the furnace.

Table II. Summary of Results of Initial Sintering Experiments

Material	Sample No.	Starting Density (% TD)	Ending Density (% TD)	T_{max} (°C)	Time at T_{max} (Min.)	Reference
Al_2O_3	1 - 1			1100	30	Figures 7d, 9b
	1 - 3	36.1	51.8	1460	10	
	1 - 4	36.7	74.2	1720	25	Figure 7e
	2 - 1	37.1	81.8	1700	70	
	2 - 3	37.4	74.8	1550	120	Figure 7f
	2 - 4	37.9	68.8	1530	180	
	2 - 8	37.3	76.2	1650	71	Figures 7g, 9c
TiO_2	1 - 1	30.0	32.6	1217	2	
	1 - 2+	32.6	38.7	1225	12	
	2	30.0	44.0	1230	60	Figures 8c, 10b
	3	30.0	52.0	1250	120	Figure 10c

+ sample heated twice

As discussed above, the casket material could be easily heated from room temperature by microwaves, thus providing a mechanism for hybrid heating. Unfortunately, hot spots often occurred in the casket material, resulting in local melting and thermal gradients near the workpiece. Some of the cracks formed in the samples during processing can be

attributed to these thermal gradients. Hot spot formation in the casket did not appear to mask the workpiece from the microwaves.
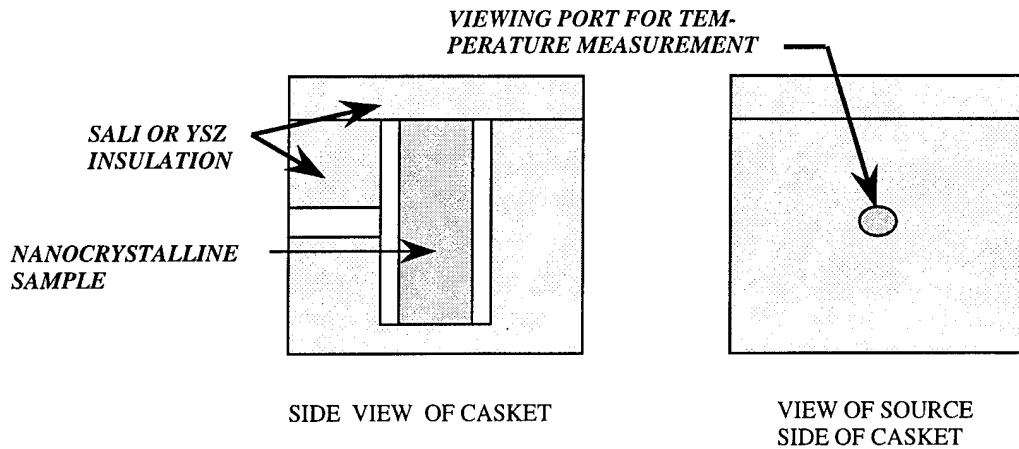

Figure 5: Schematic of casket used for insulation and hybrid heating.

Both forward and reflected power as well as the temperature were monitored for each run. A graph of all of these values for sample 2-8 is shown in Figure 6 below. The following items should be noted from these data. Initial heating of the sample was characterized by a steady decrease in the reflected power. At approximately 35 minutes elapsed time the workpiece temperature increased rapidly before stabilizing at ~ 600°C. This temperature increase was accompanied by an increase in the reflected power. This is due to the detuning of the cavity as the sample becomes a more resistive load and the cavity less of a resonant circuit. After the cavity is significantly detuned by the changes in the material, the effect of retuning the cavity with the movable short is negligible. Optimization of power input is now achieved by increasing the opening of the iris. This accounts for the marked decrease in the reflected power at approximately 45 minutes of the elapsed time. The improved coupling is accompanied by a significant increase in the sample temperature. After this, temperature increases are achieved by increasing the forward (source) power. This is especially true at the higher temperatures at which large increases in forward power are required in order to obtain modest gains in temperature (at 120–135 minutes elapsed time). The reason for this is due to radiation losses from the sample and casketing into the relatively cold walls of the cavity (which scale as $\sim T^4$). Temperature was monitored using both a single and a two-color pyrometer. There was reasonable agreement between these two sensors especially at the higher temperatures. Forward and reflected power were monitored using S-band power sensors at the forward and reflected arms of the directional couplers [see Figure 1].
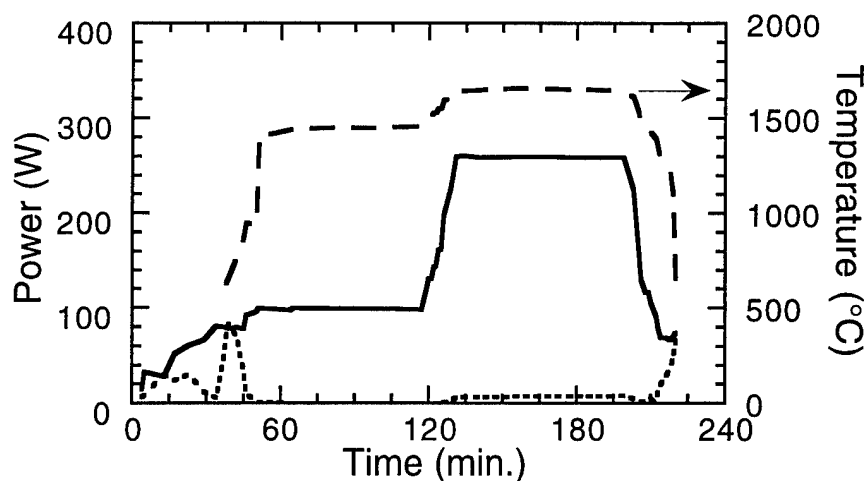
14

Figure 6: Temperature (dashed curve), forward (solid curve) and reflected (dotted curve) power profiles for microwave sintering of nanocrystalline Al_2O_3 ceramic sample 2-8.

IV.C Results and Discussion

The physical properties of the samples were investigated before and after the microwave processing. Table III shows a summary of x-ray diffraction (XRD) and scanning electron microscope (SEM) characterization of the crystalline phases formed and the average particle sizes of the oxide precursors and the final microwave treated samples. The alumina and titania x-ray diffraction data are shown in Figures 7 and 8, respectively. SEM micrographs of the alumina and titania starting materials and treated samples are shown in Figures 9 and 10, respectively. Estimates of densification were made from physical measurements.

The alumina x-ray diffraction data for the precursor powder, calcined powder, and CIP'ed green compact (curves 7a, 7b, and 7c) show broad, widely-spaced peaks characteristic of amorphous, ultra-fine grain powder. The precursor peaks are characteristic of AlOOH (Boehmite) while the calcined and CIP'ed samples manifest the γ-phase of alumina. The data for sample 1-1 (microwaved for 30 min. at 1100°C [Curve 7d]) also corresponds to the γ-phase and the XRD data indicates little grain growth, however, little densification took place during this run. Significant densification (final density~74%) did occur in sample 1-4 (microwaved at 1700°C for 254 min. [Curve 7e]), As expected, this sample shows the (high temperature) α-phase structure, as well as sharper peaks which are indicative of modest grain growth (to a grain size of ~11 nm). The XRD data for samples 2-3 and 2-8, which were heated to higher temperatures and processed for longer times, show even sharper peaks, indicating significant grain growth (grain size > 1

15

μm). The SEM data for the alumina are consistent with the XRD data. The SEM micrograph of the precursor and calcined powders (Figures 9a and 9b) show the presence of soft agglomerates. The micrograph of the sample 1-1 microwaved at 1100°C indicates a grain size ~100 nm). The micrographs of sample 2-8, processed at higher temperature (1650°C) show a relatively coarse-grained structure (grain size > 1 μm).

These data show that significant densification was generally accompanied by a substantial increase in the grain size. The one exception is sample 1-4 which achieved a density of 74% at a grain size of 11 nm. Note that the processing time for this sample was relatively short (25 minutes). The system of hybrid heating was usually successful though the problem with non-uniform heating (hot spots) caused a number of the samples to crack. In particular, the alumina results show a very good consistency between the methods used. It is evident from Figures 7d and 10c that the alumina processed at 1100°C retains the γ phase and does not transform to the α phase. Processing at higher temperatures (>1100°C) produces the characteristic α-alumina phase and, as expected, leads to significant grain growth (see SEM data in Figure 10d). The micrograph for titania sample 3 [Fig. 10c], which was held at 1200°C for 2 hours, shows a trapped spherical pore indicative of melting, as well as substantial grain growth.

Table III. Summary of ceramic phases as determined by x-ray diffraction and SEM

	As Prepared	Calcined	Microwaved	Sample
Material: Phase	TiO_2 Rutile*	TiO_2 Rutile and Anatase	TiO_2 Rutile	
Average crystallite size (Å)		200	1300	1+
			4 μm	2
			5 μm	3
Material Phase	AlOOH Boehmite	Al_2O_3 predominately γ	Al_2O_3 α above 1100°C	
Average crystallite size (Å)	< 10	< 10	20	1-1
			112	1-4
			> 1 μm	2-3
			> 1 μm	2-8

* x-ray amorphous (see Fig. 8), however, an electron diffraction pattern observed in TEM
+ see Table II for sample processing conditions

Notice the rather clean grain boundaries shown by the SEM data in Figures 9 and 10. This is indicative of a very pure starting material which partially accounts for the low final densities achieved. The low final density achieved is also due to the existence of agglomerates in the pre-sintered material. According to a theory concerning sintering in the

presence of agglomerates, high theoretical density is not reached until grain size approaches the size of the agglomerate.[14] Approaches to achieving higher final densities currently under investigation include the use of sintering aids and application of pressure during processing (sinter forging).

Methods of avoiding agglomeration during powder preparation are also being considered. The present results confirm the expectation that nanocrystalline materials couple reasonably well to 2.45 GHz microwave energy. As further evidence of this, the re-heating of partially sintered samples required more power to achieve a given temperature than the initial heating, indicating that the larger grains with their clean boundaries did not provide as much conductivity enhancement as the green compact.
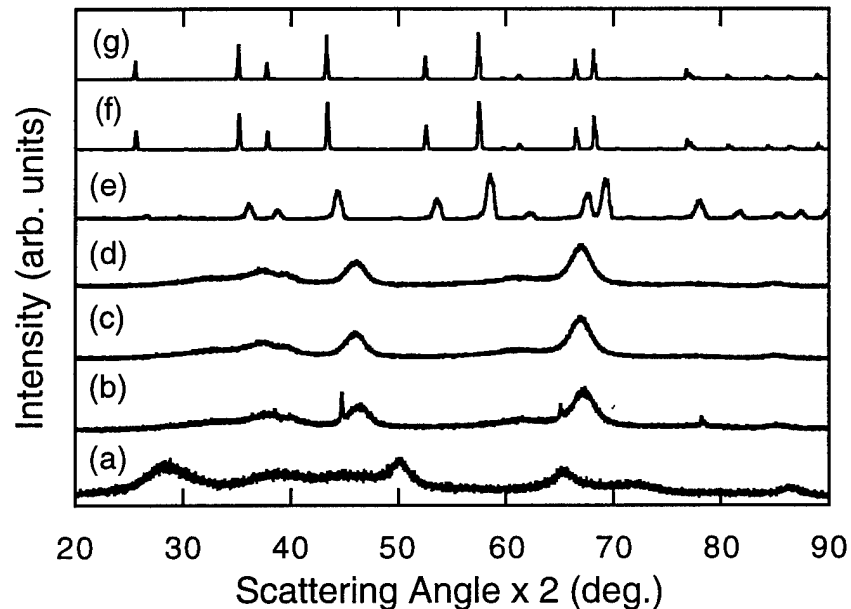

Figure 7. X-ray diffraction data for Al$_2$O$_3$ samples. Curve a: sol-gel powder; b: calcined powder; c: CIP'ed green body; d: microwaved sample 1-1 (30 min.@1100°C); e: microwaved sample 1-4 (25 min. @1720°C), f: microwaved sample 2-3 (120 min. @1550°C), g: microwaved sample 2-8 (65 min.@1450°C and 71 min. @1650°C).

The titania x-ray diffraction data for the precursor powder (Fig. 8a) is almost flat indicating an amorphous structure. The SEM micrograph for the precursor powder (Figure 10a) shows the presence of soft agglomerates. XRD data for the calcined powder (Fig. 8b), and the microwaved samples (Figs. 8c and 8d), show the peaks of the rutile crystal structure. The data for the microwaved samples are sharper than for the calcined powder, indicating that grain growth has occurred. Similarly to the alumina data, micrographs of

the microwaved titania show clean grain boundaries, triple-point pores, and pores trapped within large grains. Only modest densification was achieved, about 50% TD.
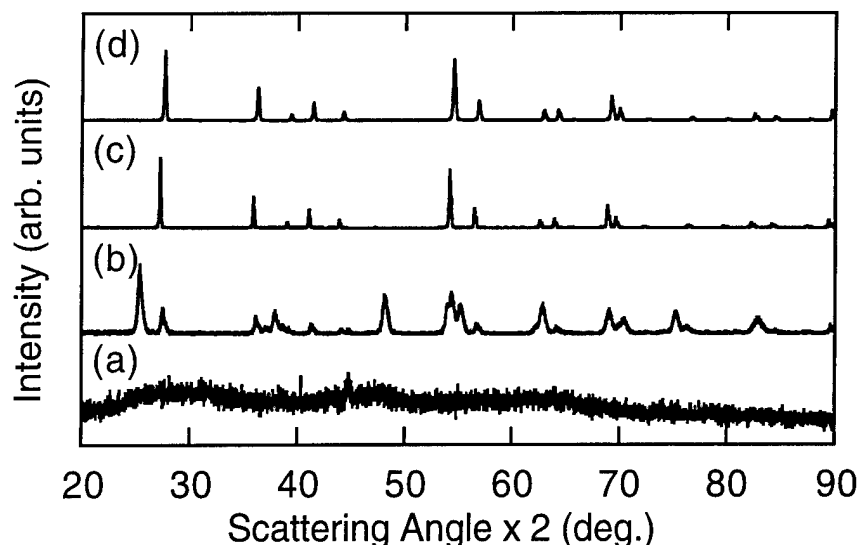

Figure 8. X-ray diffraction data for TiO_2 samples. (a) sol-gel powder; (b) calcined powder; (c) microwaved sample 2 (1 hr @ 1200 °C); and (d) microwaved sample 3 (2 hr @ 1200 °C).

V. Summary

A single-mode microwave cavity furnace has been constructed, instrumented and integrated into a microwave system that has been used to perform preliminary sintering experiments. Sintering of nanocrystalline materials up to 80% TD was achieved with moderate grain growth. Several methods of achieving higher final densities are under investigation.

VI. Acknowledgment

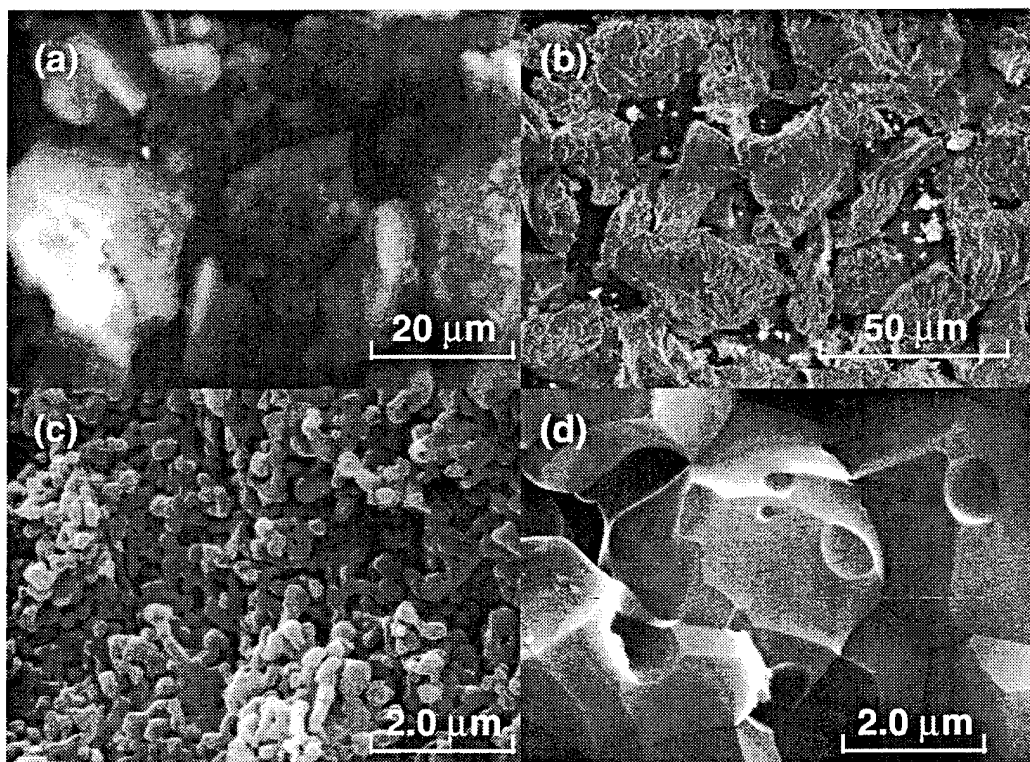This work was supported by the Office of Naval Research.

Figure 9. SEM micrographs showing the evolution of grain growth and particle size for nanocrystalline Al_2O_3. a: precursor (Boehmite) powder, b: calcined powder, c: microwaved sample 1-1, d: microwaved sample 2-8.
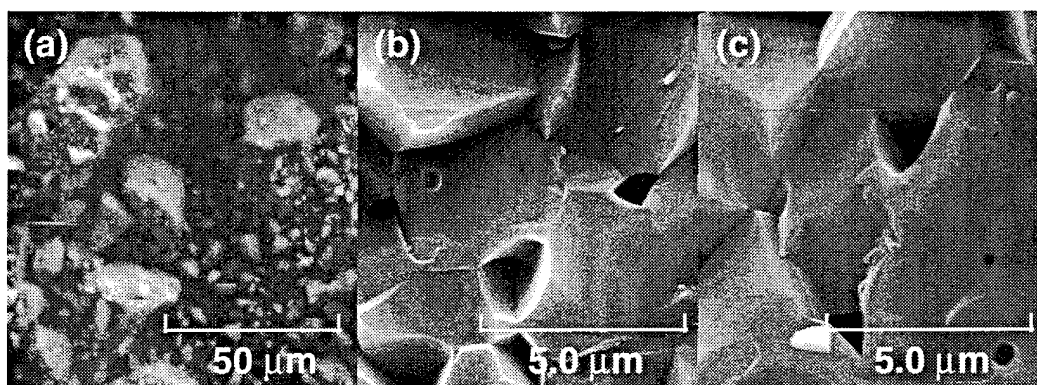

Figure 10. SEM micrographs showing the evolution of grain growth and particle size for nanocrystalline TiO_2. a: precursor powder, b: microwaved sample 2, c: microwaved sample 3. Arrow shows trapped spherical pore indicative of melting.

References

[1] *Microwave Processing of Materials*, W. H. Sutton, Guest Editor, *MRS Bulletin* **23**, No. 11, Nov. 1993.

[2] I.S. Zheludev, *Physics of Crystalline Dielectrics, Vol. 2 Electrical Properties*, (Plenum Press, New York-London, 1971), p.503.

[3] W.W. Ho, "High temperature dielectric properties of polycrystalline ceramics," *MRS Symposium Proceedings* **124**, 137 (1988).

[4] M. Aliquat, L. Mazo, and G. Desgardin, "Microwave sintering of oxides," *MRS Symposium Proceedings* **189**, 229 (1991).

[5] R. E. Collin, *Foundations for Microwave Engineering*, (McGraw-Hill, New York, 1966), p. 218.

[6] J.A. Eastman, K.E. Sickafus, J.D. Katz, S.G. Boeke, R.D. Blake, C.R. Evans, R.B. Schwarz and Y.X. Liao, "Microwave Sintering of Nanocrystalline TiO_2", MRS Symposium Proceedings, Vol. 189, pp. 273-278, Pittsburgh, PA, 1990.

[7] S.N. Kumar, A. Pant, R.R. Sood, J. Ng-Yelim and R.T. Holt, "Production of Ultra-Fine Silicon Carbide by Fast Firing in Microwave and Resistance Furnaces", Ceramic Transactions, Vol. 21, pp. 395-402, Westerville, OH, 1991.

[8] D. Vollath, R. Varma and K.E. Sickafus, "Synthesis of Nanocrystlline Powders for Oxide Ceramics by Microwave Plasma Pyrolysis", MRS Symposium Proceedings, Vol.269, pp. 379-384, Pittsburgh, PA, 1992.

[9] D. Vollath, "Some Activities of Microwave Processing of Ceramics in Germany", Ceramic Transactions, Vol. 36, pp. 147-156, Westerville, OH, 1993.

[10] J. Freim, J. McKittrick, J. Katz and K. Sickafus, "Phase Transformation and Densification Behaviour of Microwave Sintered γ-Al_2O_3", MRS Symposium Proceedings, Vol. 347, pp. 525-530, Pittsburgh, PA, 1994.

[11] J. Zhang, Y. Yang, L. Cao, S. Chen, X. Shong, and F. Xia, "Microwave Sintering on Nanocrystalline ZrO_2 Powders", MRS Symposium Proceedings, Vol. 347, pp. 591-596, Pittsburgh, PA, 1994.

[12] D. Vollath, "A Cascaded Microwave Plasma Source for Synthesis of Ceramic Nonocomposite Powders", MRS Symposium Proceedings, Vol. 347, pp. 629-634, Pittsburgh, PA, 1994.

[13] R.W. Bruce, "New Frontiers in the Use of Microwave Energy: Power and Metrology", MRS Symposium Proceedings, Vol. 124, pp. 3-15, Pittsburgh, PA, 1994.

[14] M.J. Mayo, D.C. Hague and D.-J. Chen, "Processing Nanocrystalline Ceramics for pplications in Superplasticity", Materials Science and Engineering, A166 (1993), pp. 145-159.